Concentrated beams in differentially rotating and stratified fluids and their reflection at a turning point

By Stéphane LE DIZÈS & Benjamin FAVIER

Aix Marseille Université, CNRS, Centrale Méditerranée, IRPHE, Marseille, France

(Received 6 October 2025)

Concentrated wave beams are analysed both theoretically and numerically in a general rotating and stratified axisymmetric medium, where both the rotation rate and the Brunt-Väisäla frequency vary with position. The fluid is assumed to be incompressible, weakly diffusive, and weakly viscous. The analysis is conducted within the Boussinesq approximation and a linear framework, with a prescribed frequency. An asymptotic solution is derived in the limit of weak viscosity and diffusivity, describing a harmonic wave beam localized around a characteristic (or ray path), similar to those generated by boundary singularities or critical points. This solution is shown to break down when the characteristic reaches a turning point which corresponds to the transition from oscillatory to evanescent behaviour. A local asymptotic analysis near the turning point demonstrates that the wave beam reflects, preserving its transverse structure while acquiring a phase shift of $\pm\pi/2$. These theoretical predictions are validated through numerical simulations, which show that the wave beam structure, both near and far from the turning point, is accurately reproduced.

1. Introduction

Waves are ubiquitous in rotating and stratified fluids. They play a key role in the dynamics of both the ocean (Munk & Wunsch, 1998) and the atmosphere (Fritts & Alexander, 2003). In the ocean, such waves can be generated by tidal flows interacting with topography (Wunsch, 1975). When the topography is supercritical, that is, when it has a slope tangent to the direction of wave propagation, concentrated wave beams are emitted from so-called critical (slope) points. These beams have been studied both experimentally (Zhang *et al.*, 2007; King *et al.*, 2009; Echeverri & Peacock, 2010) and theoretically (St Laurent *et al.*, 2003; Llewellyn Smith & Young, 2003; Balmforth & Peacock, 2009) in this context. Similar concentrated beams also occur in rotating fluids (Greenspan, 1968). They have often been investigated in spherical geometries (Calkins *et al.*, 2010; Koch *et al.*, 2013; Cébron *et al.*, 2019; Lin & Noir, 2021; He *et al.*, 2022, 2023) due to their relevance in planetary and stellar interiors (Le Bars *et al.*, 2015). Their structure has been examined theoretically in works such as Walton (1975); Kerswell (1995); Tilgner (2000), and more recently in Le Dizès & Le Bars (2017).

The theoretical description of these beams is based on the similarity solutions obtained by Moore & Saffman (1969) for rotating fluids and Thomas & Stevenson (1972) for stratified fluids. These asymptotic viscous solutions have primarily been used to describe wave fields far from a localised oscillating source (Hurley & Keady, 1997; Voisin, 2003; Cortet *et al.*, 2010; Machicoane *et al.*, 2015). They are parametrised by an index m,

which characterises the strength of the underlying inviscid singularity. Only recently have these solutions been applied to describe concentrated beams issued from critical points (Le Dizès & Le Bars, 2017; He *et al.*, 2022, 2023; Le Dizès, 2024). Furthermore, Ogilvie (2005) and He *et al.* (2023) have shown that these solutions can also describe the asymptotic viscous structure of the internal shear layers associated with wave attractors.

Most of the existing studies have focused on uniformly rotating and stratified fluids. In a non-uniform medium, the direction of wave propagation is expected to vary with position. In such cases, a local wave analysis is typically employed, based on WKB approximations and ray tracing techniques (Lighthill, 1978; Marks & Eckermann, 1995; Prat *et al.*, 2016; Broutman *et al.*, 2004; Prat *et al.*, 2018). This approach has helped explain various features observed in the structure of free oscillating modes in closed geometries (Baruteau & Rieutord, 2013; Guenel *et al.*, 2016; Mirouh *et al.*, 2016; Dintrans *et al.*, 1999; Mathis, 2009; Astoul *et al.*, 2021).

The concentrated beams generated from critical or singular points are small-scale structures, for which this local wave approach is expected to be applicable. We will show that the similarity solution of Moore & Saffman (1969) remains valid in a non-uniform medium, provided the beam propagates along a characteristic. The beam's width and amplitude vary according to the local properties of the medium. As it propagates, the beam may encounter a location where further propagation is no longer possible. This corresponds to a turning point where the wave transitions from oscillatory to evanescent behaviour. Mathematically, this point is also a cusp of the characteristics. We will demonstrate that the similarity solution breaks down at the turning point. A new local solution will be constructed to describe the beam behaviour near this point, showing that the beam reflects while maintaining its similarity structure and acquiring a phase shift of $\pm\pi/2$. These theoretical predictions are validated using numerical simulations of the linear governing equations.

The paper is organised as follows. Section §2 presents the general framework. We consider a non-uniform axisymmetric medium in which the angular velocity varies with the cylindrical radius and the Brunt-Väisälä frequency varies with the spherical radius. The governing equations, ray equations, and local dispersion relations are provided in this section. We also derive the form of the governing equations in the local Frenet-Serret frame attached to a given characteristic. Section §3 uses these equations to obtain an asymptotic solution describing viscous wave beams concentrated along a characteristic. The classical similarity solution of Moore & Saffman (1969) is recovered as one possible solution. Section §4 analyses the behaviour of the viscous solution near a turning point. The appropriate scalings, the local governing equation, and its solution are derived. Section §5 presents the numerical validation of the theory. Simulations are conducted in a finite domain with a non-stratified configuration, using a localised forcing to generate the concentrated beam and sponge layers to prevent boundary reflections. The structure of the solution, both near and far from the turning point, is compared with the theoretical predictions. Finally, in the conclusion, we summarise the results and discuss their possible extension to finite geometries.

2. Framework

We consider an incompressible fluid undergoing differential rotation about the vertical axis Oz, with an angular velocity $\Omega(r)$ that depends only on the cylindrical radial coordinate r. The fluid is also assumed to be stably stratified in a central gravitational field, with a Brunt-Väisälä frequency $N(\rho)$ that depends solely on the spherical radial

coordinate ρ. The kinematic viscosity ν and the scalar diffusivity α are both taken to be constant.

We are interested in harmonic, axisymmetric perturbations of frequency ϖ ($\varpi > 0$). These perturbations are described by the velocity $\mathbf{u}$, pressure P and buoyancy B, which are expressed in the form:

$$(\mathbf{U}, P, B) = (\mathbf{u}, p, b)e^{-\mathrm{i}\varpi t} + c.c. \tag{2.1}$$

where "c.c." denotes the complex conjugate. The governing equations for the amplitudes $\mathbf{u}$, p and b are derived from the Boussinesq approximation of the Navier-Stokes equations. After non-dimensionalizing all quantities using a characteristic length scale L and a characteristic velocity scale V, the linearised equations take the form:

$$-\mathrm{i}\varpi\mathbf{u} + 2\Omega(\hat{\mathbf{e}}_z \times \mathbf{u}) + r(\mathbf{u}\cdot\nabla\Omega)\hat{\mathbf{e}}_\phi = -\nabla p + b\,\hat{\mathbf{e}}_\rho + E\nabla^2\mathbf{u}, \tag{2.2a}$$

$$\nabla\cdot\mathbf{u} = 0, \tag{2.2b}$$

$$-\mathrm{i}\varpi b + N^2\mathbf{u}\cdot\hat{\mathbf{e}}_\rho = (E/Pr)\nabla^2 b, \tag{2.2c}$$

where $Pr = \nu/\alpha$ is the Prandtl number and $E = \nu/(VL)$ the Ekman number. In these equations, Ω and N now denote the rotation rate and the Brunt-Väisälä frequency non-dimensionalized by V/L. In the following, we assume $E \ll 1$ and $Pr \geq O(1)$. The cylindrical and spherical vector bases are denoted by $(\hat{\mathbf{e}}_r, \hat{\mathbf{e}}_\phi, \hat{\mathbf{e}}_z)$ and $(\hat{\mathbf{e}}_\rho, \hat{\mathbf{e}}_\theta, \hat{\mathbf{e}}_\phi)$, respectively.

2.1. *Characteristics and local dispersion relation of the non-dissipative problem*

In the non-dissipative limit ($\nu = \alpha = 0$), the system (2.2) can be reduced to a single second-order equation for the pressure p, as shown in (Mirouh *et al.*, 2016). Retaining only second-order derivatives, this equation takes the form:

$$(\varpi^2 - N^2\sin^2\theta)\frac{\partial^2 p}{\partial r^2} + 2N^2\cos\theta\,\sin\theta\frac{\partial^2 p}{\partial z\partial r} + (\varpi^2 - N^2\cos^2\theta - \xi^2)\frac{\partial^2 p}{\partial z^2} = 0, \tag{2.3}$$

where ξ is the epicyclic frequency, defined by

$$\xi^2(r) = 2\Omega(r)\omega(r), \tag{2.4}$$

and $\omega(r) = (1/r)\partial_r(r^2\Omega)$ is the background vorticity. Equation (2.3) is a generalization of the classical Poincaré equation, extended to account for both differential rotation and radial stratification. In the case of solid-body rotation and uniform stratification, it reduces to the standard form.

This equation can also be derived from the full system (2.2) in the inviscid and non-diffusive limit ($\nu = \alpha = 0$) by assuming a local plane-wave solution of the form $\exp(\mathrm{i}k_r r + \mathrm{i}k_z z)$ with $k_r \gg 1$ and $k_z \gg 1$. This leads to the local dispersion relation for inertia-gravity waves:

$$\varpi^2 = N^2\frac{(k_z\cos\theta - k_r\sin\theta)^2}{k^2} + \xi^2\frac{k_z^2}{k^2}\ , \quad k^2 = k_r^2 + k_z^2, \tag{2.5}$$

which corresponds to (2.3) under the substitution ∂_r by $\mathrm{i}k_r$ and ∂_z by $\mathrm{i}k_z$. We assume a stable configuration in which both N^2 and ξ^2 are positive. Equation (2.5) determines the allowable range of wave frequencies. At the equator ($\theta = 0$), the frequency ranges from 0 to $\sqrt{N^2+\xi^2}$, while at the poles ($\theta = \pm\pi/2$), it ranges from $\min(N,\xi)$ to $\max(N;\xi)$, depending on the relative magnitudes of N to ξ. From the dispersion relation (2.5), we can define both the phase velocity and group velocity. The phase velocity is given by

$$\mathbf{v}^{(\varphi)} = (v_r^{(\varphi)}, v_z^{(\varphi)}) = \left(\frac{\varpi k_r}{k^2}, \frac{\varpi k_z}{k^2}\right),$$

while the group velocity is

$$\mathbf{v}^{(g)} = (v_r^{(g)}, v_z^{(g)}) = \left(\frac{\partial \varpi}{\partial k_r}, \frac{\partial \varpi}{\partial k_z} \right) \tag{2.6}$$

with explicit expressions:

$$v_r^{(g)} = -k_z \frac{N^2 k_\rho k_\theta + \xi^2 k_r k_z}{\varpi} \ , \quad v_z^{(g)} = k_r \frac{N^2 k_\rho k_\theta + \xi^2 k_r k_z}{\varpi}, \tag{2.7}$$

where

$$k_\rho = k_r \cos\theta + k_z \sin\theta, \quad k_\theta = -k_r \sin\theta + k_z \cos\theta.$$

The paths of characteristics associated with equation (2.3) are given by

$$\frac{dz}{dr} = \frac{N^2 \sin\theta\cos\theta \pm \sqrt{\Delta}}{\varpi^2 - N^2 \sin^2\theta}, \tag{2.8a}$$

$$\frac{dr}{dz} = \frac{N^2 \sin\theta\cos\theta \mp \sqrt{\Delta}}{\varpi^2 - N^2 \cos^2\theta - \xi^2}, \tag{2.8b}$$

where

$$\Delta = \varpi^2(N^2 + \xi^2 - \varpi^2) - N^2 \xi^2 \sin^2\theta. \tag{2.9}$$

The curves defined by the vanishing of Δ correspond to turning points, which play a key role in the wave dynamics. These curves separate regions where equation (2.3) is hyperbolic ($\Delta > 0$) from those where it is elliptic ($\Delta < 0$). Only the hyperbolic regions ($\Delta \geq 0$) are relevant for wave propagation, as they admit characteristic paths. In a non-stratified fluid ($N = 0$), turning points occur at cylindrical locations where $\varpi = \xi(r)$. At these points, the ray path becomes horizontal. Conversely, in a non-rotating fluid ($\Omega = 0$) or in a potential fluid ($\omega = 0$), the turning points lie at the spherical locations where $\varpi = N(\rho)$. At these points, the ray path becomes radial.

Moreover, the slope of the characteristic can be related to the group velocity. From equation (2.10), we have:

$$\frac{v_z^{(g)}}{v_r^{(g)}} = -\frac{k_r}{k_z} = \frac{N^2 \sin\theta\cos\theta \pm \sqrt{\Delta}}{\varpi^2 - N^2 \sin^2\theta} \ , \tag{2.10}$$

indicating that the group velocity points in the direction of the characteristic paths. Using the dispersion relation (2.5), the expression (2.9) for Δ can also be rewritten as:

$$\Delta = (N^2 k_\rho k_\theta + \xi^2 k_r k_z)^2. \tag{2.11}$$

This expression implies that the group velocity (2.7) vanishes precisely when $\Delta = 0$, i.e., at turning points.

2.2. *Local Frenet-Serret frame*

Consider a characteristic path $\mathcal{C}$ parametrized by an arclength $x_\parallel > 0$ that increases in the direction of wave propagation. At any point along the path, the position vector is given by

$$\mathbf{x}_0(x_\parallel) = r_0(x_\parallel)\hat{\mathbf{e}}_r + z_0(x_\parallel)\hat{\mathbf{e}}_z.$$

We define a local Frenet-Serret frame $(\hat{\mathbf{e}}_\parallel, \hat{\mathbf{e}}_\perp)$ in the (r, z) plane as follows:

$$\frac{\partial \mathbf{x}_0}{\partial x_\parallel} = \hat{\mathbf{e}}_\parallel(x_\parallel) = r_0'(x_\parallel)\hat{\mathbf{e}}_r + z_0'(x_\parallel)\hat{\mathbf{e}}_z \ , \quad \hat{\mathbf{e}}_\perp = -z_0'(x_\parallel)\hat{\mathbf{e}}_r + r_0'(x_\parallel)\hat{\mathbf{e}}_z. \tag{2.12}$$

The vectors $\hat{\mathbf{e}}_\parallel$ and $\hat{\mathbf{e}}_\perp$ are orthonormal and satisfy the standard Frenet-Serret relations:

$$\frac{\partial \hat{\mathbf{e}}_\parallel}{\partial x_\parallel} = \kappa(x_\parallel)\hat{\mathbf{e}}_\perp(x_\parallel) \ , \quad \frac{\partial \hat{\mathbf{e}}_\perp}{\partial x_\parallel} = -\kappa(x_\parallel)\hat{\mathbf{e}}_\parallel(x_\parallel), \tag{2.13}$$

where $\kappa(x_\parallel)$ is the curvature of the characteristic path $\mathcal{C}$ at the point $\mathbf{x}_0(x_\parallel)$. It is given by

$$\kappa(x_\parallel) = z_0''(x_\parallel)r_0'(x_\parallel) - r_0''(x_\parallel)z_0'(x_\parallel) \ . \tag{2.14}$$

The characteristic path $\mathbf{x_0}(x_\parallel)$ satisfies the dispersion relation, which can be written as

$$\varpi^2 = \xi_0^2(r_0')^2 + N_0^2\frac{(r_0r_0' + z_0z_0')^2}{\rho_0^2}, \tag{2.15}$$

where $\rho_0 = \sqrt{r_0^2 + z_0^2}$ is the local spherical radius, and $\xi_0 = \xi(r_0)$, $N_0 = N(\rho_0)$. The function $\Delta(x_\parallel)$ can also be expressed along the characteristic path using equation (2.9) as:

$$\Delta(x_\parallel) = \varpi^2(N_0^2 + \xi_0^2 - \varpi^2) - N_0^2\xi_0^2z_0^2/\rho_0^2. \tag{2.16}$$

Another useful expression for Δ, derived from the dispersion relation (2.15), is

$$\Delta(x_\parallel) = \frac{\left(N_0^2(r_0r_0' + z_0z_0')(r_0z_0' - z_0r_0') + \xi_0^2r_0'z_0'\rho_0^2\right)^2}{\rho_0^4}. \tag{2.17}$$

This allows us to write

$$\epsilon_1\sqrt{\Delta} = \frac{N_0^2(r_0r_0' + z_0z_0')(r_0z_0' - z_0r_0')}{\rho_0^2} + \xi_0^2r_0'z_0' \tag{2.18}$$

where $\epsilon_1 = \mathrm{sgn}[N_0^2(r_0r_0' + z_0z_0')(r_0z_0' - z_0r_0') + \xi_0^2r_0'z_0'\rho_0^2]$. From this, we can derive the following additional expressions:

$$z_0'/r_0' = \frac{N_0^2r_0z_0/\rho_0^2 + \epsilon_1\sqrt{\Delta}}{\varpi^2 - N_0^2z_0^2/\rho_0^2}, \tag{2.19a}$$

$$r_0'/z_0' = \frac{N_0^2r_0z_0/\rho_0^2 - \epsilon_1\sqrt{\Delta}}{\varpi^2 - \xi_0^2 - N_0^2r_0^2/\rho_0^2}. \tag{2.19b}$$

The characteristic path $\mathcal{C}$ may reach a turning point $\mathbf{x}_c = (r_c, z_c)$ at a specific value $x_{\parallel c}$ of the arclength parameter $x_\parallel$, where $\Delta = 0$. At this point, the characteristic path terminates and reflects, as illustrated in figure 1. It exhibits a generic cusp structure, which can be explicitly calculated under the assumption that the root of Δ is simple, that is,

$$\Delta(x_{\parallel c}) = \Delta_c = 0 \ \text{ and } \ \Delta'(x_{\parallel c}) = \Delta_c' \neq 0.$$

Let us now investigate the form of the path in the local frame $(\hat{\mathbf{e}}_{\parallel c}, \hat{\mathbf{e}}_{\perp c})$ attached to the turning point $\mathbf{x}_c$ (see figure 1(a)). If we express the path as $\mathbf{x}_0 = \mathbf{x}_c + y_{\parallel 0}\hat{\mathbf{e}}_{\parallel c} + y_{\perp 0}\hat{\mathbf{e}}_{\perp c}$, the coordinates $(y_{\parallel 0}, y_{\perp 0})$ satisfy, for $x_\parallel$ close to $x_{\parallel c}$

$$y_{\parallel 0} \sim -|x_\parallel - x_{\parallel c}| \ , \quad y_{\perp 0} \sim \pm\frac{2}{3}\alpha_c|x_\parallel - x_{\parallel c}|^{3/2}, \tag{2.20}$$

which leads to the following relation between $y_{\perp 0}$ and $y_{\parallel 0}$:

$$y_{\perp 0} \sim \pm\frac{2}{3}\alpha_c(-y_{\parallel 0})^{3/2}. \tag{2.21}$$

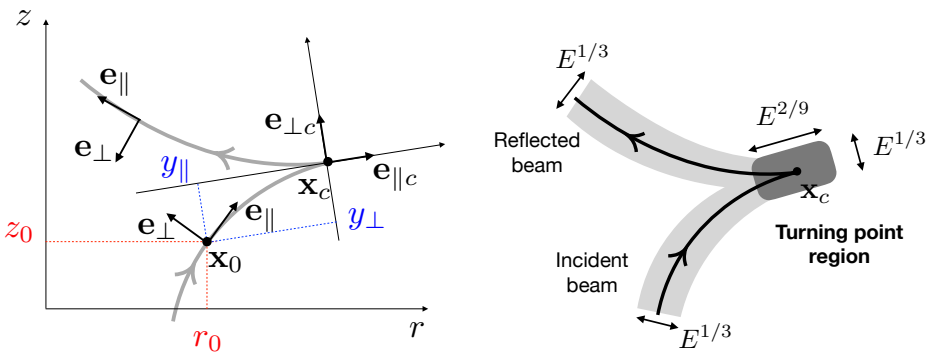

(a) (b)

FIGURE 1. (a) Frames associated with the characteristic path close to a turning point $\mathbf{x}_c$. (b) Scaling of the turning point region for a viscous beam.

Here, α_c is given by

$$\alpha_c = -\frac{\epsilon_1 z_c'^2\sqrt{-\Delta_c'}}{\varpi^2-\xi_c^2-N_c^2r_c^2/\rho_c^2} = -\frac{\epsilon_1 r_c'^2\sqrt{-\Delta_c'}}{\varpi^2-N_c^2z_c^2/\rho_c^2} = -\frac{\epsilon_1\sqrt{-\Delta_c'}}{2\varpi^2-N_c^2-\xi_c^2}, \tag{2.22}$$

where the subscript c denotes values evaluated at the turning point $x_{\parallel c}$. In equations (2.20b) and (2.21), the upper sign corresponds to the incident beam ($x_\parallel < x_{\parallel c}$) while the lower sign corresponds to the reflected beam ($x_\parallel > x_{\parallel c}$). If $N_c^2 r_c z_c \neq 0$, none of the denominators in (2.22) vanish, since

$$(\varpi^2-\xi_c^2-N_c^2r_c^2/\rho_c^2)(\varpi^2-N_c^2z_c^2/\rho_c^2) = N_c^4r_c^2z_c^2/\rho_c^4 > 0,$$

and

$$2\varpi^2-\xi_c^2-N_c^2 = (\varpi^2-\xi_c^2-N_c^2r_c^2/\rho_c^2)+(\varpi^2-N_c^2z_c^2/\rho_c^2).$$

If $N_c^2 r_c z_c = 0$, then either $r_c' = 0$ and $\varpi^2-\xi_c^2-N_c^2r_c^2/\rho_c^2 = 0$, or $z_c' = 0$ and $\varpi^2 - N_c^2z_c^2/\rho_c^2 = 0$. In either case, the third expression of α_c remains valid.

It is important to note that the vectors $\hat{\mathbf{e}}_\perp$ and $\hat{\mathbf{e}}_\parallel$ associated with the reflected beam do not match $\hat{\mathbf{e}}_{\perp c}$ and $\hat{\mathbf{e}}_{\parallel c}$ as $x_\parallel \to x_{\parallel c}$. As a result, the functions r_0' and z_0' are not continuous across $x_{\parallel c}$. Throughout this analysis, all quantities evaluated at $x_{\parallel c}$ should be understood as taken in the limit $x_\parallel \to x_{\parallel c}^-$, i.e., for the incident beam.

Finally, it is interesting to note that the curvature κ also diverges at $\mathbf{x}_c$ as

$$\kappa \sim -\frac{\alpha_c}{2\sqrt{|x_{\parallel c}-x_\parallel|}}. \tag{2.23}$$

2.3. *Governing equations in the local frame of the characteristics*

As we are interested in solutions localized around the characteristic path $\mathcal{C}$, it is useful to express the governing equations in the local coordinate system associated with this path. We define the local variables $(x_\parallel, x_\perp)$ of a point $\mathbf{x}$ close to $\mathcal{C}$ by writing:

$$\mathbf{x} = \mathbf{x}_0(x_\parallel) + x_\perp\hat{\mathbf{e}}_\perp\ , \quad \text{with} \quad \mathbf{x}_0(x_\parallel) = r_0(x_\parallel)\hat{\mathbf{e}}_r + z_0(x_\parallel)\hat{\mathbf{e}}_z, \tag{2.24}$$

where $\mathbf{x}_0(x_\parallel)$ is the closest point to $\mathbf{x}$ on $\mathcal{C}$. The differential vector increment can then be expressed as

$$\begin{aligned} d\mathbf{x} &= \frac{\partial\mathbf{x}_0}{\partial x_\parallel}dx_\parallel + \frac{\partial\mathbf{x}_0}{\partial\phi}d\phi + x_\perp\frac{\partial\hat{\mathbf{e}}_\perp}{\partial x_\parallel}dx_\parallel + \hat{\mathbf{e}}_\perp dx_\perp \\ &= (1-\kappa x_\perp)dx_\parallel\hat{\mathbf{e}}_\parallel + dx_\perp\hat{\mathbf{e}}_\perp + r_0 d\phi\,\hat{\mathbf{e}}_\phi. \end{aligned} \tag{2.25}$$

which ensures that $(x_\parallel, x_\perp, \phi)$ forms an orthogonal curvilinear coordinate system with the metric components $(h_\parallel, h_\perp, h_\phi) = (1 - \kappa(x_\parallel)x_\perp, 1, r_0(x_\parallel))$.

The governing equations (2.2) become, in this local coordinate system:

$$-\mathrm{i}\varpi u_\parallel - 2\Omega(r) r_0' u_\phi = -\frac{1}{h_\parallel}\frac{\partial p}{\partial x_\parallel} + b\,\hat{\mathbf{e}}_\rho \cdot \hat{\mathbf{e}}_\parallel + E(\nabla^2 \mathbf{u})_\parallel, \quad (2.26a)$$

$$-\mathrm{i}\varpi u_\perp + 2\Omega(r) z_0' u_\phi = -\frac{\partial p}{\partial x_\perp} + b\,\hat{\mathbf{e}}_\rho \cdot \hat{\mathbf{e}}_\perp + E(\nabla^2 \mathbf{u})_\perp, \quad (2.26b)$$

$$-\mathrm{i}\varpi u_\phi + \omega(r)(r_0' u_\parallel - z_0' u_\perp) = E(\nabla^2 \mathbf{u})_\phi, \quad (2.26c)$$

$$\frac{\partial (r_0 u_\parallel)}{\partial x_\parallel} + r_0 \frac{\partial (h_\parallel u_\perp)}{\partial x_\perp} = 0, \quad (2.26d)$$

$$-\mathrm{i}\varpi b + N^2(\rho)(u_\parallel\, \hat{\mathbf{e}}_\rho \cdot \hat{\mathbf{e}}_\parallel + u_\perp\, \hat{\mathbf{e}}_\rho \cdot \hat{\mathbf{e}}_\perp) = (E/Pr)\nabla^2 b, \quad (2.26e)$$

with the geometric relations:

$$\hat{\mathbf{e}}_\rho \cdot \hat{\mathbf{e}}_\parallel = \frac{r_0 r_0' + z_0 z_0'}{\rho}\ , \quad \hat{\mathbf{e}}_\rho \cdot \hat{\mathbf{e}}_\perp = \frac{z_0 r_0' - r_0 z_0' + x_\perp}{\rho}, \quad (2.27)$$

and the coordinate transformations:

$$r = r_0 - z_0' x_\perp\ , \quad z = z_0 + r_0' x_\perp\ , \quad \rho = \sqrt{r^2 + z^2}. \quad (2.28)$$

3. Viscous solutions localized around a characteristic path

In this section, we develop an approximation for a viscous/diffusive solution that is localized on the characteristic path $\mathcal{C}$. Our goal is to extend the solutions derived by Moore & Saffman (1969) and Thomas & Stevenson (1972), originally obtained for purely rotating or purely stratified fluid, to the more general case of a non-uniformly rotating and stratified fluid.

Guided by their approach, we introduce a stretched transverse coordinate:

$$\bar{x}_\perp = \frac{x_\perp}{E^{1/3}}, \quad (3.1)$$

and make the following ansatz:

$$u_\parallel = u_\parallel^{(0)}(x_\parallel, \bar{x}_\perp) + \ldots, \quad (3.2a)$$

$$u_\perp = E^{1/3} u_\perp^{(1)}(x_\parallel, \bar{x}_\perp) + \ldots, \quad (3.2b)$$

$$u_\phi = u_\phi^{(0)}(x_\parallel, \bar{x}_\perp) + \ldots, \quad (3.2c)$$

$$b = b^{(0)}(x_\parallel, \bar{x}_\perp) + \ldots, \quad (3.2d)$$

$$p = E^{1/3} p^{(1)}(x_\parallel, \bar{x}_\perp) + \ldots. \quad (3.2e)$$

From equations (2.26c,e), the leading-order relations between $u_\parallel^{(0)}$, $u_\phi^{(0)}$ and $b^{(0)}$ are:

$$u_\phi^{(0)} = -\frac{\mathrm{i}\omega_0 r_0'}{\varpi} u_\parallel^{(0)}, \quad (3.3a)$$

$$b^{(0)} = -\frac{\mathrm{i}N_0^2}{\varpi}\frac{r_0 r_0' + z_0 z_0'}{\rho_0} u_\parallel^{(0)}, \quad (3.3b)$$

with $\rho_0 = \sqrt{r_0^2 + z_0^2}$, where, we recall, $N_0 = N(\rho_0)$ and $\omega_0 = \omega(r_0)$. From the leading

order balance of equation (2.26b), we obtain:

$$\frac{\partial p^{(1)}}{\partial \bar{x}_\perp} = -2\Omega_0 z_0' u_\phi^{(0)} - \frac{r_0 z_0' - z_0 r_0'}{\rho_0} b^{(0)}.$$

Substituting expressions from (3.3a,b) yields

$$\frac{\partial p^{(1)}}{\partial \bar{x}_\perp} = \frac{\mathrm{i}}{\varpi}\left(\xi_0^2 r_0' z_0' + N_0^2 \frac{(r_0 r_0' + z_0 z_0')(r_0 z_0' - z_0 r_0')}{\rho_0^2}\right) u_\parallel^{(0)}. \tag{3.4}$$

Now consider the operation $\mathrm{i}\varpi$(2.26a) $-2\Omega_0 r_0'$(2.26c) - $(r_0 r_0' + z_0 z_0')/\rho_0$(2.26e), which gives:

$$\begin{aligned}\left(\varpi^2 - \xi_0^2 (r_0')^2 - N_0^2 \frac{(r_0 r_0' + z_0 z_0')^2}{\rho_0^2}\right) u_\parallel^{(0)} \\ = -E^{1/3}\left(\xi_0^2 r_0' z_0' + N_0^2 \frac{(r_0 r_0' + z_0 z_0')(r_0 z_0' - z_0 r_0')}{\rho_0^2}\right) u_\perp^{(1)} - \mathrm{i}E^{1/3}\varpi \frac{\partial p^{(1)}}{\partial x_\parallel} \\ + E^{1/3}\left(\mathrm{i}\varpi \frac{\partial^2 u_\parallel^{(0)}}{\partial \bar{x}_\perp^2} - 2\Omega_0 r_0' \frac{\partial^2 u_\phi^{(0)}}{\partial \bar{x}_\perp^2} - \frac{1}{Pr}\frac{(r_0 r_0' + z_0 z_0')}{\rho_0}\frac{\partial^2 b^{(0)}}{\partial \bar{x}_\perp^2}\right).\end{aligned} \tag{3.5}$$

The left-hand side vanishes due to the dispersion relation (2.15). Taking the derivative with respect to $\bar{x}_\perp$ and substituting $\partial_{\bar{x}_\perp} p^{(1)}$ from (3.4), $u_\phi^{(0)}$ and $b^{(0)}$ from (3.3a,b), and using the expression for $\partial_{\bar{x}_\perp} u_\perp^{(1)}$ from equation (2.26d):

$$\frac{\partial u_\perp^{(1)}}{\partial \bar{x}_\perp} = -\frac{1}{r_0}\frac{\partial (r_0 u_\parallel^{(0)})}{\partial x_\parallel}, \tag{3.6}$$

we finally obtain a single equation for $u_\parallel^{(0)}$:

$$\begin{aligned}\left(\xi_0^2 r_0' z_0' + N_0^2 \frac{(r_0 r_0' + z_0 z_0')(r_0 z_0' - z_0 r_0')}{\rho_0^2}\right)\frac{1}{r_0}\frac{\partial (r_0 u_\parallel^{(0)})}{\partial x_\parallel} = \\ -\frac{\partial}{\partial x_\parallel}\left[\left(\xi_0^2 r_0' z_0' + N_0^2 \frac{(r_0 r_0' + z_0 z_0')(r_0 z_0' - z_0 r_0')}{\rho_0^2}\right) u_\parallel^{(0)}\right] \\ -\frac{\mathrm{i}}{\varpi}\left(2\xi_0^2 (r_0')^2 + \left(1 + \frac{1}{Pr}\right) N_0^2 \frac{(r_0 r_0' + z_0 z_0')^2}{\rho_0^2}\right)\frac{\partial^3 u_\parallel^{(0)}}{\partial \bar{x}_\perp^3}.\end{aligned} \tag{3.7}$$

If we now introduce the new function $\tilde{u}_\parallel$ and the new variable $\tilde{x}_\parallel$ defined by

$$u_\parallel^{(0)}(\bar{x}_\perp, x_\parallel) = r_0^{-1/2}\left|\xi_0^2 r_0' z_0' + N_0^2 \frac{(r_0 r_0' + z_0 z_0')(r_0 z_0' - z_0 r_0')}{\rho_0^2}\right|^{-1/2} \tilde{u}_\parallel(\bar{x}_\perp, \tilde{x}_\parallel), \tag{3.8a}$$

$$\tilde{x}_\parallel = \int_{x_\parallel^{(0)}}^{x_\parallel} \frac{2\xi_0^2 (r_0')^2 \rho_0^2 + (1 + Pr^{-1}) N_0^2 (r_0 r_0' + z_0 z_0')^2}{2\varpi(\xi_0^2 r_0' z_0' \rho_0^2 + N_0^2 (r_0 r_0' + z_0 z_0')(r_0 z_0' - z_0 r_0'))} + \tilde{x}_\parallel^{(0)}, \tag{3.8b}$$

then equation (3.7) becomes the parameter-free equation

$$\frac{\partial \tilde{u}_\parallel}{\partial \tilde{x}_\parallel} = -\mathrm{i}\frac{\partial^3 \tilde{u}_\parallel}{\partial \bar{x}_\perp^3}. \tag{3.9}$$

In equation (3.8b), the parameter $x_\parallel^{(0)} > 0$ corresponds to the arclength at which we start considering the solution, and $\tilde{x}_\parallel^{(0)}$ is an arbitrary constant.

Equation (3.9) is the same as the one obtained by Moore & Saffman (1969) and Thomas & Stevenson (1972). It can be easily solved using a Fourier transform in $\bar{x}_\perp$, yielding a general solution:

$$\tilde{u}_\parallel = \int_{-\infty}^{\infty} a(k) e^{-k^3 \tilde{x}_\parallel} e^{\mathrm{i}k\bar{x}_\perp} dk. \tag{3.10}$$

In the denominator of equation (3.8b), we recognize the expression (2.18) for $\epsilon_1\sqrt{\Delta}$. For $x_\parallel > x_\parallel^{(0)}$, the sign of $\tilde{x}_\parallel$ depends on the value of ϵ_1. The solutions propagating along $\mathcal{C}$ in the direction of increasing $x_\parallel$ consist of positive wavenumbers ($a(k<0)=0$) if $\epsilon_1 = 1$, and negative wavenumbers ($a(k>0)=0$) if $\epsilon_1 = -1$. Hence, the solutions propagating along $\mathcal{C}$ in the direction of increasing $x_\parallel$ can be written as

$$\tilde{u}_\parallel = \int_{0}^{\infty} b(k) e^{-k^3 \epsilon_1 \tilde{x}_\parallel} e^{\mathrm{i}k\epsilon_1\bar{x}_\perp} dk. \tag{3.11}$$

When the incident beam reaches the turning point $x_{\parallel c}$, the viscous solution given by (3.8a,b) and (3.11) breaks down, as the amplitude prefactor in the expression (3.8a) for $u_\parallel^{(0)}$ diverges. While the denominator in $\tilde{x}_\parallel$ in (3.8b) vanishes at this point, the integral remains convergent. The behavior near the turning point can be obtained by taking $x_\parallel \to x_{\parallel c}$ in (3.8a,b). We obtain:

$$u_\parallel^{(0)} \sim r_c^{-1/2} \left|-\Delta_c'(x_{\parallel c} - x_\parallel)\right|^{-1/4} \tilde{u}_\parallel(\bar{x}_\perp, \tilde{x}_{\parallel c}). \tag{3.12}$$

This expression can be written in terms of the local variable $(y_\parallel, y_\perp)$ when $x_\parallel \to x_{\parallel c}$ using the approximations

$$x_{\parallel c} - x_\parallel \sim -y_{\parallel 0} = -y_\parallel \ , \quad x_\perp \sim y_\perp - y_{\perp 0} \sim y_\perp - \frac{2}{3}\alpha_c(-y_\parallel)^{3/2}. \tag{3.13}$$

Since $x_\perp = O(E^{1/3})$, the second relation implies that $y_\perp = O(E^{1/3})$ and $y_\parallel = O(E^{2/9})$ in the vicinity of the turning point. We will use this scaling to analyse the behavior of the solution near the turning point region in the next section.

Note that, in expression (3.11), if we choose

$$b(k) = b^S(k) \equiv k^{m-1} \frac{e^{-\mathrm{i}m\pi/2}}{(m-1)!} \ , \quad \text{with} \ \ m > 0, \tag{3.14}$$

we recover the similarity solution derived by Moore & Saffman (1969) and Thomas & Stevenson (1972):

$$\tilde{u}_\parallel = \tilde{u}_\parallel^S \equiv |\tilde{x}_\parallel|^{-m/3} h_m(\eta) \ , \quad \eta = \epsilon_1 \frac{\bar{x}_\perp}{|\tilde{x}_\parallel|^{1/3}}, \tag{3.15}$$

where the function $h_m(\eta)$ is defined as

$$h_m(\eta) = \frac{e^{-\mathrm{i}m\pi/2}}{(m-1)!} \int_0^\infty e^{-p^3} e^{\mathrm{i}p\eta} p^{m-1} dp. \tag{3.16}$$

The normalization of the function h_m ensures the following asymptotic behavior:

$$h_m(\eta) \underset{\eta\to+\infty}{\sim} |\eta|^{-m}, \tag{3.17a}$$

$$h_m(\eta) \underset{\eta\to-\infty}{\sim} e^{-\mathrm{i}m\pi} |\eta|^{-m}. \tag{3.17b}$$

This implies that the similarity solution $\tilde{u}_\parallel^S$ behaves as

$$\tilde{u}_\parallel^S \underset{\epsilon_1 \bar{x}_\perp \to +\infty}{\sim} |\bar{x}_\perp|^{-m}, \tag{3.18a}$$

$$\tilde{u}_\parallel^S \underset{\epsilon_1 \bar{x}_\perp \to -\infty}{\sim} e^{-\mathrm{i}m\pi} |\bar{x}_\perp|^{-m}. \tag{3.18b}$$

These behaviours demonstrate that expression (3.15) defines a viscous solution associated with an inviscid singularity of the form $|x_\perp|^{-m}$ along the characteristic path $\mathcal{C}$. The definition (3.15) of the similarity variable η shows that this singularity originates at $\tilde{x}_\parallel = 0$. The width of the wave beam is given by $|\tilde{x}_\parallel|^{1/3}$, where $\tilde{x}_\parallel$ evolves according to (3.8b).

4. Solution close to the turning point and reflected beam

We have seen in the previous section that the solution described by (3.8a,b) and (3.11) breaks down upon reaching a turning point. In this section, our objective is to derive a new approximation that remains valid in the vicinity of a turning point. To this end, we adopt the local frame $(\hat{\mathbf{e}}_{\parallel c}, \hat{\mathbf{e}}_{\perp c})$ and the local coordinates $(y_\parallel, y_\perp)$.

In this frame, if we denote the velocity components along $\hat{\mathbf{e}}_{\parallel c}$ and $\hat{\mathbf{e}}_{\perp c}$ by $v_\parallel$ and $v_\perp$, respectively, the governing equations become:

$$-\mathrm{i}\varpi v_\parallel - 2\Omega r_c' u_\phi = -\frac{\partial p}{\partial y_\parallel} + b\,\hat{\mathbf{e}}_\rho \cdot \hat{\mathbf{e}}_{\parallel c} + E\nabla^2 v_\parallel, \tag{4.1a}$$

$$-\mathrm{i}\varpi v_\perp + 2\Omega z_c' u_\phi = -\frac{\partial p}{\partial y_\perp} + b\,\hat{\mathbf{e}}_\rho \cdot \hat{\mathbf{e}}_{\perp c} + E\nabla^2 v_\perp, \tag{4.1b}$$

$$-\mathrm{i}\varpi u_\phi + \omega(r_c' v_\parallel - z_c' v_\perp) = E\nabla^2 u_\phi, \tag{4.1c}$$

$$\frac{\partial r v_\parallel}{\partial y_\parallel} + r\frac{\partial v_\perp}{\partial y_\perp} = 0, \tag{4.1d}$$

$$-\mathrm{i}\varpi b + N^2(v_\parallel\,\hat{\mathbf{e}}_\rho \cdot \hat{\mathbf{e}}_{\parallel c} + v_\perp\,\hat{\mathbf{e}}_\rho \cdot \hat{\mathbf{e}}_{\perp c}) = (E/Pr)\nabla^2 b. \tag{4.1e}$$

We now introduce the following ansatz:

$$v_\parallel = v_\parallel^{(0)},\ v_\perp = E^{1/9} v_\perp^{(1)},\ u_\phi = u_\phi^{(0)},\ b = b^{(0)},\ p = E^{4/9} p^{(4)}, \tag{4.2}$$

together with the rescaled local variables:

$$\bar{y}_\parallel = E^{-2/9} y_\parallel\ ,\quad \bar{y}_\perp = E^{-1/3} y_\perp. \tag{4.3}$$

Under this scaling, the governing equations reduce to:

$$-\mathrm{i}\varpi v_\parallel^{(0)} - 2\Omega r_c' u_\phi^{(0)} = -E^{2/9}\frac{\partial p^{(4)}}{\partial \bar{y}_\parallel} + b^{(0)}(r r_c' + z z_c')/\rho, \tag{4.4a}$$

$$-\mathrm{i}\varpi E^{1/9} v_\perp^{(1)} + 2\Omega z_c' u_\phi^{(0)} = -E^{1/9}\frac{\partial p^{(4)}}{\partial \bar{y}_\perp} + b^{(0)}(z r_c' - r z_c')/\rho, \tag{4.4b}$$

$$-\mathrm{i}\varpi u_\phi^{(0)} + \omega(r_c' v_\parallel^{(0)} - z_c' v_\perp^{(1)} E^{1/9}) = 0, \tag{4.4c}$$

$$\frac{\partial v_\parallel^{(0)}}{\partial \bar{y}_\parallel} + \frac{\partial v_\perp^{(1)}}{\partial \bar{y}_\perp} = 0, \tag{4.4d}$$

$$-\mathrm{i}\varpi b^{(0)} + (N^2/\rho)(v_\parallel^{(0)}(r r_c' + z z_c') + E^{1/9} v_\perp^{(1)}(z r_c' - r z_c')) = 0. \tag{4.4e}$$

Note that viscous terms do not appear in these equations.

From equations (4.4c,e), we express $u_\phi^{(0)}$ and $b^{(0)}$ in terms of $v_\parallel^{(0)}$ and $v_\perp^{(1)}$:

$$u_\phi^{(0)} = \frac{\omega}{\mathrm{i}\varpi}(r_c' v_\parallel^{(0)} - z_c' E^{1/9} v_\perp^{(1)}), \tag{4.5a}$$

$$b^{(0)} = \frac{N^2}{\mathrm{i}\varpi\rho}(v_\parallel^{(0)}(rr_c' + zz_c') - E^{1/9} v_\perp^{(1)}(rz_c' - zr_c')). \tag{4.5b}$$

Substituting these into equations (4.4a,b) yields:

$$-\frac{\Delta_c'}{\mathrm{i}\varpi(2\varpi^2 - \xi_c^2 - N_c^2)}\bar{y}_\parallel v_\parallel^{(0)} = -\frac{\partial p^{(4)}}{\partial \bar{y}_\parallel}, \tag{4.6a}$$

$$\frac{2\varpi^2 - \xi_c^2 - N_c^2}{\mathrm{i}\varpi} v_\perp^{(1)} = -\frac{\partial p^{(4)}}{\partial \bar{y}_\perp}, \tag{4.6b}$$

where we have used the following estimates, deduced from equations (2.15), (2.16) and (2.17) near the turning point r_c:

$$2\Omega\omega r_c' z_c' + N^2(rr_c' + zz_c)(rz_c' - zr_c')/\rho^2 = O(E^{2/9}),$$

$$-\varpi^2 + 2\Omega\omega z_c'^2 + N^2(rz_c' - zr_c')^2/\rho^2 \sim -2\varpi^2 + \xi_c^2 + N_c^2,$$

$$-\varpi^2 + 2\Omega\omega r_c'^2 + N^2(rr_c' + zz_c')^2/\rho^2 \sim E^{2/9}\frac{\Delta_c'}{2\varpi^2 - \xi_c^2 - N_c^2}\bar{y}_\parallel.$$

Elimating $p^{(4)}$ and $v_\perp^{(1)}$ using (4.4d) finally gives a single equation for $v_\parallel^{(0)}$

$$\frac{\partial^2 v_\parallel^{(0)}}{\partial \bar{y}_\parallel^2} - \frac{\Delta_c'\,\bar{y}_\parallel}{(2\varpi^2 - \xi_c^2 - N_c^2)^2}\frac{\partial^2 v_\parallel^{(0)}}{\partial \bar{y}_\perp^2} = 0. \tag{4.7}$$

This equation can be solved using a Fourier transform in the $\bar{y}_\perp$ direction:

$$v_\parallel^{(0)} = \int_{-\infty}^{+\infty} \tilde{v}_\parallel e^{\mathrm{i}k\bar{y}_\perp} dk \tag{4.8}$$

such that $\tilde{v}_\parallel$ satisfies the Airy equation

$$\frac{\partial^2 \tilde{v}_\parallel}{\partial \tilde{y}_\parallel^2} - \tilde{y}_\parallel \tilde{v}_\parallel = 0, \tag{4.9}$$

with

$$\tilde{y}_\parallel = \gamma |k|^{2/3} \bar{y}_\parallel, \tag{4.10}$$

and

$$\gamma = \left(\frac{-\Delta_c'}{(2\varpi^2 - \xi_c^2 - N_c^2)^2}\right)^{1/3}, \tag{4.11}$$

The solution that remains bounded for large $|\tilde{y}_\parallel|$ is

$$\tilde{v}_\parallel = c(k)\mathrm{Ai}\left(\tilde{y}_\parallel\right), \tag{4.12}$$

where Ai is an Airy function (Abramowitz & Stegun, 1965, p. 446), and $c(k)$ is a function to be determined by matching.

Using the asymptotic expansion of the Airy function as $\tilde{y}_\parallel \to -\infty$ (Abramowitz &

Stegun, 1965, p. 448), we obtain:

$$\tilde{v}_\parallel \sim \frac{c(k)}{\sqrt{\pi}(-\tilde{y}_\parallel)^{1/4}} \sin\left(\frac{2}{3}(-\tilde{y}_\parallel)^{3/2} + \frac{\pi}{4}\right). \tag{4.13}$$

This leads to the following asymptotic form for $v_\parallel^{(0)}$:

$$\begin{aligned} v_\parallel^{(0)} \sim \int_{-\infty}^{+\infty} \frac{C(k)}{(-\bar{y}_\parallel)^{1/4}} \Bigg\{ &\exp\left[\mathrm{i}k\left(\bar{y}_\perp + \frac{2|k|}{3k}\gamma^{3/2}(-\bar{y}_\parallel)^{3/2}\right) - \mathrm{i}\pi/4\right] \\ &+ \exp\left[\mathrm{i}k\left(\bar{y}_\perp - \frac{2|k|}{3k}\gamma^{3/2}(-\bar{y}_\parallel)^{3/2}\right) + \mathrm{i}\pi/4\right]\Bigg\} dk, \end{aligned} \tag{4.14}$$

with

$$C(k) = \frac{c(k)}{2\sqrt{\pi}\gamma^{1/4}|k|^{1/6}}. \tag{4.15}$$

This expression is a sum of four wave beams, corresponding to positive and negative wavenumbers propagating along two paths: $\bar{y}_\perp = \frac{2}{3}\gamma^{3/2}(-\bar{y}_\parallel)^{3/2}$ and $\bar{y}_\perp = -\frac{2}{3}\gamma^{3/2}(-\bar{y}_\parallel)^{3/2}$. Only one of these corresponds to the incident beam. Using (3.12) and (3.13), the expression for the incident beam in terms of the local variable is

$$u_\parallel^{(0)} \sim \frac{\displaystyle\int_0^{+\infty} b(k) e^{-k^3\epsilon_1\tilde{x}_{\parallel c}} e^{\mathrm{i}k\epsilon_1(\bar{y}_\perp - \frac{2}{3}\alpha_c(-\bar{y}_\parallel)^{3/2})} dk}{r_c^{1/2}(-\Delta_c')^{1/4}(-\bar{y}_\parallel)^{1/4}E^{1/18}}\ . \tag{4.16}$$

From (2.22), we can write

$$\alpha_c = -\epsilon_1\epsilon_2\gamma^{3/2}, \tag{4.17}$$

with $\epsilon_2 = \mathrm{sgn}(2\varpi^2 - \xi_c^2 - N_c^2)$. We then immediately see that the incident beam corresponds to the second term in (4.14) if $\epsilon_2 > 0$, but to the first term if $\epsilon_2 < 0$. The condition of matching then imposes that the following relation between $C(k)$ in (4.14) and $b(k)$ in (4.16):

$$C(k) = \frac{H(\epsilon_1 k) b(\epsilon_1 k)}{r_c^{1/2}(-\Delta_c')^{1/4}E^{1/18}} e^{-k^3\tilde{x}_{\parallel c}} e^{\mathrm{i}\epsilon_2\pi/4}, \tag{4.18}$$

where $H(z)$ is the Heaviside function.

Expression (4.18) for $C(k)$ implies the following expression for $c(k)$ appearing in (4.12):

$$c(k) = \frac{H(\epsilon_1 k) b(\epsilon_1 k) 2\sqrt{\pi}\gamma^{1/4}|k|^{1/6}}{r_c^{1/2}(-\Delta_c')^{1/4}E^{1/18}} e^{-k^3\tilde{x}_{\parallel c}} e^{\mathrm{i}\epsilon_2\pi/4}. \tag{4.19}$$

For the similarity solution obtained with $b(k)$ given by (3.14), we obtain the following expression for the solution in the turning point region:

$$v_\parallel = C_t V_m^S(Y_\parallel, Y_\perp), \tag{4.20}$$

where

$$V_m^S(Y_\parallel, Y_\perp) \equiv \int_0^\infty k^{m-1+1/6}\mathrm{Ai}(k^{2/3}Y_\parallel) e^{\mathrm{i}kY_\perp} e^{-k^3} dk, \tag{4.21}$$

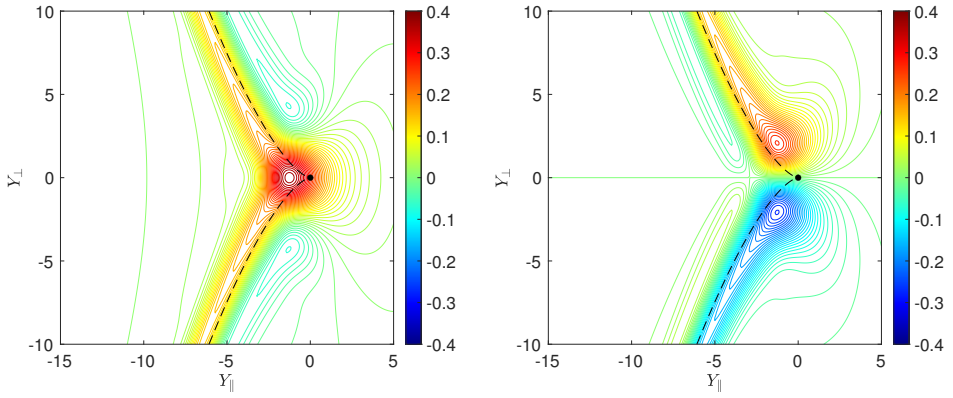

FIGURE 2. Contour plot of the function V_m^S in the $(Y_\parallel, Y_\perp)$ plane for $m = 1$. Dashed black lines indicate the ray trajectory ($Y_\perp = \pm(-Y_\parallel)^{3/2}$) as it reflects at the turning point (black circle at the origin). (a) Real part of V_m^S. (b) Imaginary part of V_m^S.

and

$$C_t = \frac{2\sqrt{\pi}\gamma^{1/4}}{\tilde{x}_{\parallel c}^{(m+1/6)/3} r_c^{1/2} (-\Delta_c')^{1/4} E^{1/18}} \frac{e^{-\mathrm{i}m\pi/2}}{(m-1)!} e^{\mathrm{i}\epsilon_2 \pi/4} \ , \tag{4.22a}$$

$$Y_\parallel = \frac{\gamma y_\parallel}{|\tilde{x}_{\parallel c}|^{2/9} E^{2/9}} \ , \tag{4.22b}$$

$$Y_\perp = \frac{\epsilon_1 y_\perp}{|\tilde{x}_{\parallel c}|^{1/3} E^{1/3}} \ . \tag{4.22c}$$

We recall that γ is defined in (4.11), Δ in (2.9), and $\tilde{x}_\parallel$ in (3.8b).

Contour plots of the real and imaginary parts of the function V_1^S in the $(Y_\parallel, Y_\perp)$ plane are shown in figure 2. The real part $\Re e(V_m^S)$ is even with respect to the variable $Y_\perp$ while the imaginary part $\Im m(V_m^S)$ is odd in $Y_\perp$. Both functions are localized around the ray trajectory defined by $Y_\perp = \pm(-Y_\parallel)^{3/2}$ for $Y_\parallel \leq 0$. For positive $Y_\parallel$, both functions become evanescent, i.e., they decay exponentially as $Y_\parallel$ increases, consistent with the known behavior of the Airy function Ai for positive arguments. This agrees with the physical expectation that no waves propagate beyond the turning point located at the origin.

The other term in (4.14) corresponds to the reflected beam. It has the same form as the incident beam expression (4.16), but it is now localized along the path $\bar{y} = -(2/3)\alpha_c(-\bar{y}_\parallel)^{3/2}$. If we express this term in the coordinates associated with the reflected beam, which is such that $\hat{\mathbf{e}}_\parallel$ and $\hat{\mathbf{e}}_\perp$ are reversed compared to those of the incident beam (see figure 1), we obtain

$$u_{\parallel R}^{(0)} \sim -\frac{e^{\mathrm{i}\epsilon_2\pi/2} \displaystyle\int_0^{+\infty} b(k) e^{-k^3\epsilon_1 \tilde{x}_{\parallel c}} e^{\mathrm{i}k\epsilon_1(\bar{y}_\perp + \frac{2}{3}\alpha_c(-\bar{y}_\parallel)^{3/2})} dk}{r_c^{1/2}(-\Delta_c')^{1/4}(-\bar{y}_\parallel)^{1/4} E^{1/18}} \ . \tag{4.23}$$

This yields an expression for the reflected beam of the same form as (3.8) as we move

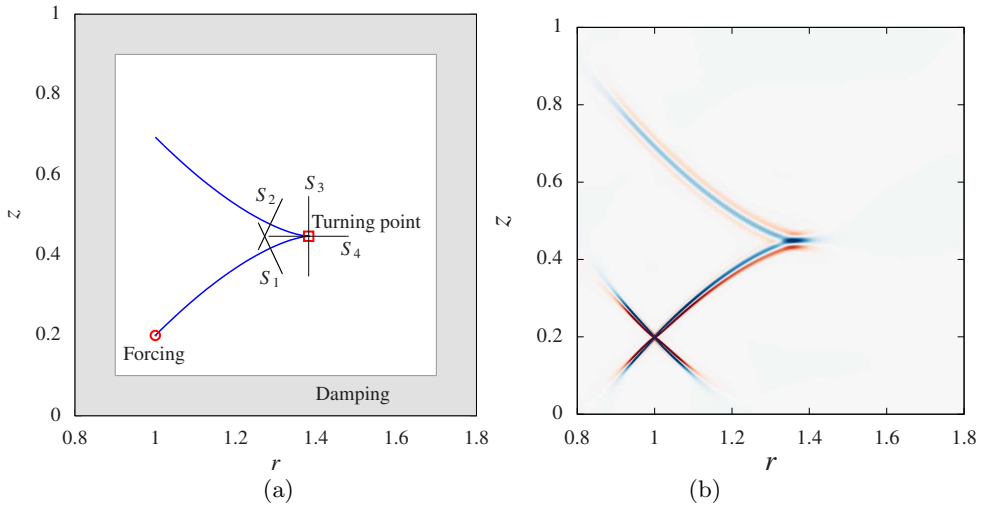

FIGURE 3. (a) Schematic of the numerical domain. The blue line shows the ray path from the forcing point (red circle) across the turning point (red square) and the ensuing reflected beam. Slices from S_1 to S_4 correspond to the locations where the comparisons between asymptotics and numerics are performed. The gray area is the damping region necessary to prevent reflections on the boundaries. (b) Transverse velocity U_ϕ once the harmonic response is reached for $E = 10^{-7}$. A movie showing the time evolution of the global solution and the rescaled local solution can be found in Supplemental materials.

away from the turning point:

$$u^{(0)}_{\|R}(\bar{x}_\perp, x_\parallel) = r_0^{-1/2} \left| \xi^2 r_0' z_0' + N^2 \frac{(r_0 r_0' + z_0 z_0')(r_0 z_0' - z_0 r_0')}{\rho_0^2} \right|^{-1/2} \tilde{u}_{\|R}(\bar{x}_\perp, \tilde{x}_\parallel), \quad (4.24a)$$

$$\tilde{x}_\parallel = \int_{x_{\|c}}^{x_\parallel} \frac{2\xi^2 (r_0')^2 \rho_0^2 + (1 + Pr^{-1}) N^2 (r_0 r_0' + z_0 z_0')^2}{2\varpi (\xi^2 r_0' z_0' \rho_0^2 + N^2 (r_0 r_0' + z_0 z_0')(r_0 z_0' - z_0 r_0'))} + \tilde{x}_{\|c}, \quad (4.24b)$$

where $\tilde{u}_{\|R}(\bar{x}_\perp, \tilde{x}_\parallel)$ is given by

$$\tilde{u}_{\|R} = e^{-\mathrm{i}\epsilon_2 \pi/2} \int_0^\infty b(k) e^{-k^3 \epsilon_1 \tilde{x}_\parallel} e^{-\mathrm{i}k\epsilon_1 \bar{x}_\perp} dk. \quad (4.25)$$

This matches the form of the incident beam expression in (3.11), if we replace $\bar{x}_\perp$ by $-\bar{x}_\perp$ and include a phase shift of $-\epsilon_2 \pi/2$. Note that the sign of this phase shift is given by the sign of $N^2 + \xi^2 - 2\varpi^2$ at the turning point. For a non-stratified fluid $\varpi = \xi_c$ and for a non-rotating or potential flow, $\varpi = N_c$. In both cases, this sign is negative ($\epsilon_2 = 1$), so the phase shift is $-\pi/2$.

5. Comparison with numerical simulations

In this section, we compare the asymptotic predictions of the previous sections with numerical simulations of the linear viscous problem. We consider a non-stratified fluid ($N = 0$) that is rotating with a non-uniform angular velocity profile $\Omega(r)$. As in the theoretical analysis, the problem is assumed to be axisymmetric about the rotation axis, and we use cylindrical coordinates (r, z). We focus on the wave dynamics generated by localized forcing at a point (r_f, z_f) within a finite radial interval (r_i, r_o) distant from the axis (i.e. $r_i > 0$).

Instead of solving the harmonic perturbation equations (2.2), we solve the time-dependent linearized equations for the perturbations in the rotating frame with an external forcing term:

$$\frac{\partial \mathbf{U}}{\partial t} + 2\Omega(\hat{\mathbf{e}}_z \times \mathbf{U}) + r(\mathbf{U}\cdot\nabla\Omega)\hat{\mathbf{e}}_\phi = -\nabla P + E\nabla^2\mathbf{U} + \boldsymbol{f} - \frac{\chi}{\tau}\mathbf{U}, \tag{5.1a}$$

$$\nabla\cdot\mathbf{U} = 0, \tag{5.1b}$$

where $\mathbf{U}$ and P are the perturbation velocity and pressure, respectively. The radius r_f and the local rotation rate $\Omega(r_f)$ are used to non-dimensionalize the variables. The Ekman number is then defined as $E = \nu/(\Omega(r_f)r_f^2)$. Note that, as before, we have used the same notation Ω for both the dimensional and dimensionless rotation rates.

The external forcing $\boldsymbol{f}$ in equation (5.1a) is prescribed as

$$\boldsymbol{f} = \sin(\varpi t)\exp(-(R/R_0)^2)\hat{\mathbf{e}}_\phi, \tag{5.2}$$

with $R = \sqrt{(r-1)^2 + (z-z_f)^2)}$ is the distance from the forcing point located at $(1, z_f)$, and R_0 is the characteristic size of the forcing region. We choose R_0 small enough for the forcing to be considered nearly point-like, while still allowing the numerical resolution of the inner viscous structure of the fluid response around that point. Typically, we choose $R_0 = 10^{-3}$. Note that this forcing procedure does not give direct access to the structure of the emitted shear layer, in particular we cannot control the singularity strength given by the parameter m in equation (3.16). As shown below, our particular forcing procedure leads to a shear layer which is accurately modeled as a Moore and Saffman beam with $m = 2$.

Since we solve these equations in a finite square domain $[r_i, r_o] \times [z_i, z_o]$ with no-slip boundary conditions on all sides, we add the last term in equation (5.1a) in order to prevent reflections at the boundaries of the domain. This relaxation term ensures a fast decay of waves before they can reach and reflect on the boundaries. The function χ is zero in the bulk of the domain and reaches unity as soon as the distance from the walls is 10^{-1} or less, as indicated in gray in figure 3. The parameter τ is chosen to ensure a gradual absorption of the waves and minimise reflected waves, typically $\tau = 4$ (larger values lead to reflection from the damping layer itself while smaller values lead to waves reflecting from the boundaries).

In the following, we use the following set of parameters. The numerical domain is defined by $r_i = 0.8$ and $r_o = 1.8$ while the vertical extent is $z \in [0, 1]$. The forcing is centered at $(r_f, z_f) = (1, 0.2)$. The rotation rate of the fluid is non-uniform and varies linearly with the horizontal coordinate according to

$$\Omega(r) = 1 - \alpha(r-1). \tag{5.3}$$

Note that this linear variation of the rotation rate is only valid away from the rotation axis. The differential rotation parameter α must be carefully chosen: it must ensure that a turning point lies within the computational domain, while also avoiding centrifugal instability. The latter condition is satisfied by requiring $\xi^2(r) > 0$ throughout the domain, where ξ is the epicyclic frequency defined in equation (2.4). For the linear rotation profile defined in equation (5.3), both constraints are satisfied over the radial domain $r \in [0.8, 1.8]$ with $\alpha = 1/2$. The Ekman number is fixed to $E = 10^{-7}$ and the wave frequency is set to $\varpi = \sqrt{3/2}$, so that the initial propagation angle at the forcing point is 45°. Finally, the remaining parameters are $R_0 = 10^{-3}$, which defines the size of the forcing region, and $\tau = 4$, which sets the damping timescale in the outer sponge layer to effectively suppress boundary reflections.

We solve this initial value problem using the open-source spectral element solver

Nek5000 (Fischer, 1997; Deville *et al.*, 2002), which allows for local mesh refinement around the forcing region and the turning point. The domain is discretised using a number $\mathcal{E} = 10404$ of hexahedral elements while the velocity is discretised within each element using Lagrange polynomial interpolants of order 14. No dealiasing is used since the equations solved are effectively linear. Convergence has been tested by gradually increasing the polynomial order for a fixed number of elements. We focus on the time-harmonic solution obtained after the initial transient has decayed.

Our analysis focuses on the wave beam emitted from the source located at (r_f, z_f), propagating toward the upper-right quadrant of the domain, see figure 3(a) and (b). The equation of the characteristic along which the beam is localized, is derived from (2.8) and takes the form

$$z'(r) = \frac{dz}{dr} = \frac{\sqrt{\Delta}}{\varpi^2} = \sqrt{5 - 5r + r^2}. \tag{5.4}$$

Integrating this expression yields the path of the characteristic

$$z(r) = \frac{3}{4} + \left(-\frac{5}{4} + \frac{r}{2}\right)\sqrt{5 - 5r + r^2} - \frac{5}{8}\log\left(5 - 2r - 2\sqrt{5 - 5r + r^2}\right) + z_f, \tag{5.5}$$

shown in blue in figure 3(a). The turning point is located at $r_c = (5 - \sqrt{5})/2$. For the present forcing, the structure of the beam is found to be well-described by a Moore-Saffman solution with singularity index $m = 2$. The evolution of this solution along the characteristic is described by equations (3.8), (3.11), (3.14), which lead to the following expression for the parallel velocity component:

$$u_\parallel \sim A\frac{C_0(r)}{|\tilde{x}_\parallel|^{2/3}} h_2(\eta) \quad , \quad \eta = \frac{x_\perp}{(E\tilde{x}_\parallel)^{1/3}} \tag{5.6}$$

where

$$C_0(r) = \frac{1}{\varpi\sqrt{rz'(r)}} = \sqrt{\frac{2}{3}}\frac{1}{\sqrt{r}(5 - 5r + r^2)^{1/4}}, \tag{5.7a}$$

$$\tilde{x}_\parallel = \int_{x_\parallel^{(0)}}^{x_\parallel} \frac{dx_\parallel}{\varpi z'(r)} + \tilde{x}_\parallel^{(0)} = \sqrt{\frac{2}{3}}\int_1^r \sqrt{\frac{6 - 5r + r^2}{5 - 5r + r^2}}dr + \tilde{x}_\parallel^{(0)}. \tag{5.7b}$$

The azimuthal velocity u_ϕ is related to $u_\parallel$ via equation (3.3a):

$$u_\phi = -\mathrm{i}C_1(r)u_\parallel, \tag{5.8}$$

with

$$C_1(r) = \frac{\omega(r)}{\varpi\sqrt{1 + z'^2}} = \sqrt{\frac{3}{2}}\frac{(2 - r)}{\sqrt{6 - 5r + r^2}} \ . \tag{5.9}$$

The physical azimuthal velocity is then given by

$$U_\phi(t) = 2|A|\frac{C_0(r)C_1(r)}{|\tilde{x}_\parallel|^{2/3}}\Re e\left(h_2(\eta)e^{-\mathrm{i}(\varpi t - \phi_A + \pi/2)}\right). \tag{5.10}$$

When the beam reaches the turning point, the approximation (4.20) with $m = 2$ has to be used:

$$u_\parallel \sim AC_tV_2(Y_\parallel, Y_\perp). \tag{5.11}$$

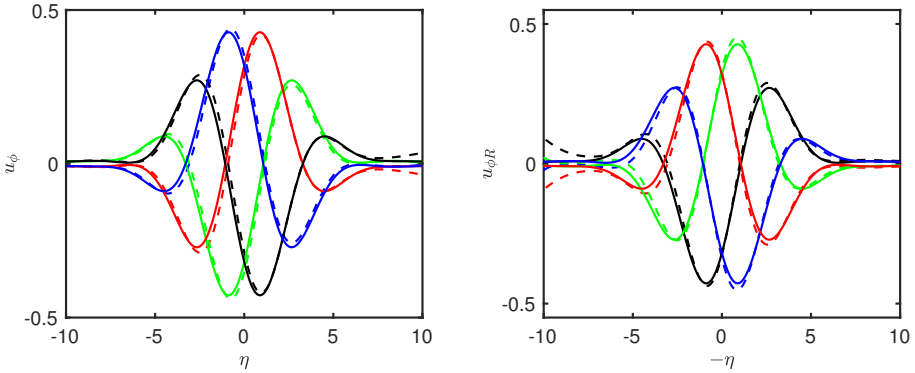

FIGURE 4. Structure of incident and reflected beams. Plot of $U_\phi(t_N)$, $N = 0, 1, 2, 3$ normalized by $M = 2|A|C_0C_1/(\tilde{x}_\parallel)^{2/3}$, as a function of the rescaled transverse variable $\eta = x_\perp/(E\tilde{x}_\parallel)^{1/3}$, in section S_1 for the incident beam (a), in section S_2 for the reflected beam (b), as shown in figure 3(a). Both $\tilde{x}_\parallel$ and M are evaluated at r_1, corresponding to the radial coordinate of the crossing point of the critical beam with sections S_1 and S_2. The solid lines represent the theoretical solutions, while the dashed lines correspond to the numerical results. The colors indicate different times: $t = t_0$ (blue), $t = t_1$ (red), $t = t_2$ (green) and $t = t_3$ (black). In these plots, $|A| = 0.087$ and $\tilde{x}_\parallel^{(0)} = 0.25$.

The amplitude C_t, and local variables $Y_\parallel$ and $Y_\perp$, are defined in this case by:

$$C_t = -\frac{4\sqrt{\pi}}{5^{1/12}\sqrt{3(5-\sqrt{5})}}\frac{e^{\mathrm{i}\pi/4}}{\tilde{x}_{\parallel c}^{13/18}E^{1/18}} \approx -2.1531\frac{e^{\mathrm{i}\pi/4}}{\tilde{x}_{\parallel c}^{13/18}E^{1/18}}\ , \tag{5.12a}$$

$$Y_\parallel = \frac{5^{1/6}(r-r_c)}{|\tilde{x}_{\parallel c}|^{2/9}E^{2/9}}\ , \tag{5.12b}$$

$$Y_\perp = \frac{(z-z_c)}{|\tilde{x}_{\parallel c}|^{1/3}E^{1/3}}\ . \tag{5.12c}$$

The physical azimuthal velocity near the turning point is then given by:

$$U_\phi(t) = 2|A||C_t|C_1(r_t)\Re e\left(V_2(Y_\parallel, Y_\perp)e^{-\mathrm{i}(\varpi t-\phi_A-3\pi/4)}\right). \tag{5.13}$$

The reflected beam has a similar expression to the incident beam, but we have to change $x_\perp$ in $-x_\perp$ and add a phase shift of $-\pi/2$. Moreover, the relation between $u_\parallel$ and u_ϕ is now $u_\phi = \mathrm{i}C_1u_\parallel$, so we obtain

$$U_{\phi R}(t) = 2|A|\frac{C_0(r)C_1(r)}{|\tilde{x}_\parallel|^{2/3}}\Re e\left(h_2(-\eta)e^{-\mathrm{i}(\varpi t-\phi_A)}\right). \tag{5.14}$$

The functions C_0 and C_1 remain unchanged for the reflected beam. However, the coordinate $\tilde{x}_\parallel$ differs, and is now given by:

$$\tilde{x}_\parallel = \sqrt{\frac{2}{3}}\int_r^{r_c}\sqrt{\frac{6-5r+r^2}{5-5r+r^2}}dr + \hat{x}_{\parallel c} + \tilde{x}_\parallel^{(0)}. \tag{5.15}$$

where

$$\hat{x}_{\parallel c} = \sqrt{\frac{2}{3}}\int_1^{r_c}\sqrt{\frac{6-5r+r^2}{5-5r+r^2}}dr \approx 0.7468. \tag{5.16}$$

Once the singularity index m is known, the theoretical solution still involves three

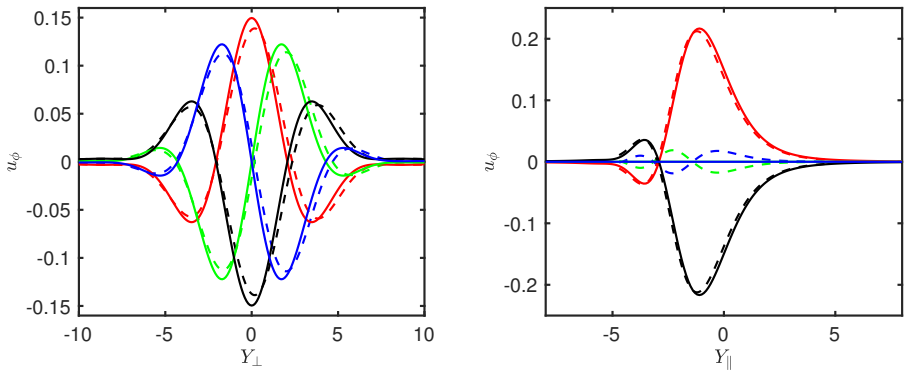

FIGURE 5. Structure of the solution in the turning point region. Plot of $U_\phi(t_N)$, $N = 0, 1, 2, 3$ normalized by $2|A|C_tC_1(r_t)$ in the vertical section S_3 (a) as a function of $Y_\perp$ and in the horizontal section S_4 (b) as a function of $Y_\parallel$, see figure 3(a). As in figure 4, the solid lines represent the theoretical solutions and the dashed lines the numerical results. The colors correspond to the same times as before: $t = t_0$ (blue), $t = t_1$ (red), $t = t_2$ (green) and $t = t_3$ (black). The parameters $|A| = 0.087$ and $\tilde{x}_\parallel^{(0)} = 0.25$ are also the same as in figure 4.

unknown parameters: the phase ϕ_A, the amplitude $|A|$ and the initial value $\tilde{x}_\parallel^{(0)}$ of $\tilde{x}_\parallel$. Once these parameters are determined, the solution is fully specified for all time. For the comparison, we select four distinct times $t_N = t_o + N\pi/(2\varpi), N = 0, 1, 2, 3$ spanning one oscillation period. The reference time t_o and phase ϕ_A are chosen such that

$$\max_{r_1<r<r_2, z=z_c} |U_\phi(t_o)|$$

is the smallest together with the condition that $U_\phi(t_1) > 0$ at the turning point. Theoretically, the first condition is satisfies if $e^{-\mathrm{i}(\varpi t_o - \phi_A - 3\pi/4)} = \pm\mathrm{i}$ since $V_2(Y_\parallel, 0)$ is real for all $Y_\parallel$. The second condition implies that the positive sign must be chosen, which determines the phase as $\varpi t_o - \phi_A = \pi/4$. The remaining two parameters are obtained by fitting the amplitude and width of the expression $\sqrt{u_\phi^2(t_0) + u_\phi^2(t_1)}$ for the incident beam in section S_1, shown in figure 3(a).

Figure 4 compares the numerical results with the theoretical solution for both incident and reflected beams. We observe very good agreement at all four times t_N. The reflected beams curves display the expected phase shift: the structure of the reflected beam at time t_N corresponds to the one of the incident beam at time t_{N-1}.

The solution in the turning point region is shown in figure 5 in both a vertical section (a) and a horizontal section (b) (sections S_3 and S_4 shown in figure 3(a)). Again, we observe good agreement between the numerical solution and the theoretical prediction. Note however, that the numerical solution in the horizontal section does not vanish for $t = t_0$ and $t = t_2$, in contrast to the theoretical solution. Capturing this variation would require incorporating higher-order corrections into the theoretical model.

6. Conclusion

In this work, we have shown that concentrated viscous wave beams can still be described by the solution introduced by Moore & Saffman (1969), even when the fluid is non-uniformly rotating and non-uniformly stratified. The wave beam follows the ray path obtained from the equation of characteristics, but its properties vary with the local

conditions of the fluid. Explicit expressions for the beam width and amplitude have been derived by solving the governing equations in a reference frame attached to the characteristic. When the characteristic reaches a turning point, the amplitude diverges. To describe the wave beam in the neighbourhood of this point, a new asymptotic solution has been derived, which, as expected, takes the form of Airy functions. Matching this local solution with the incident wave beam allows us to fully describe the local behavior and demonstrates that a reflected beam is generated with the same structure as the incident beam. However, the reflected beam has experienced a $\pm\pi/2$ phase shift relative to the incident beam. The sign of the phase shift for the $u_\parallel$ component is determined by the sign of the quantity $N^2+\xi^2-2\varpi^2$ evaluated at the turning point. In the cases of a non-stratified or non-rotating fluid, this sign is always negative so the phase shift is $-\pi/2$. These results have been validated by direct numerical simulation for a non-uniformly rotating case.

It is important to note that the effect of reflection at a turning point on the viscous beam is very similar to the effect of a reflection at the rotation axis. In both cases, the viscous beam acquires a $\pm\pi/2$ phase shift but undergoes no contraction or expansion. This contrasts with reflections at inclined boundaries, where viscous beams are expected to either contract or expand depending on the boundary inclination angle during reflection, but without gaining any phase shift. However, the sign of the phase shift on the axis depends on another quantity: for the $u_\parallel$ component, it is determined by the sign of $N^2-\xi^2$ (see, for instance He *et al.*, 2022).

These findings could be useful to extend results obtained for a uniformly rotating fluid in a bounded domain. In He *et al.* (2022, 2023, 2025), it was shown that an asymptotic solution can be constructed for an uniformly rotating fluid in a spherical shell geometry by propagating viscous wave beams generated at critical points on the inner core. Two scenarios were considered in this bounded domain: (1) when the ray paths form a periodic circuit, and (2) when they converge towards attractors. In the first case, it was shown that the sum formed by the superposition of the infinitely many contributions from the critical point beam traveling along the periodic circuit is finite, provided there is a phase shift along the circuit. In the second case, the situation was reverse: an asymptotic solution close to the attractor was derived, but only if no phase shift occurs along the attractor. In a non-uniformly rotating medium, similar results may be expected. Suppose the ray path emitted from a singularity (a critical point or a corner) generates a periodic circuit as it reflects on boundaries, axes and turning points. The viscous beam created by the singularity will travel on the same path indefinitely. As for the uniformly rotating case, a finite solution arises only if the sum of all contributions converges. This requires a net phase shift along the periodic circuit, which depends on the cumulative phase shifts acquired at each reflection, at turning points or axes. A similar argument applies to attractors. However, for the theory developed in He *et al.* (2023, 2025) to hold, the total phase shift around the circuit must vanish. This situation can occurs, for example, when there are four reflections at turning points along the attractor, a configuration observed in (Mirouh *et al.*, 2016, figure 6(c)).

Declaration of Interests. The authors report no conflict of interest.

References

Abramowitz, M. & Stegun, I. A. 1965 *Handbook of Mathematical Functions*. New York: Dover.

Astoul, A., Park, J., Mathis, S., Baruteau, C. . & Gallet, F. 2021 The complex interplay between tidal inertial waves and zonal flows in differentially rotating stellar and planetary convective regions. I. Free waves. *A & A* **647**, A144.

Balmforth, N. & Peacock, T. 2009 Tidal conversion by supercritical topography. *J. Phys. Oceano.* pp. 1965–74.

Baruteau, C. & Rieutord, M. 2013 Inertial waves in a differential rotating spherical shell. *J. Fluid Mech.* **719**, 47–81.

Broutman, D., Rottman, J. W. & Eckermann, S. D. 2004 Ray methods for internal waves in the atmosphere and ocean. *Annu. Rev. Fluid Mech.* **36**, 233–253.

Calkins, M. A., Noir, J., Eldredge, J. D. & Aurnou, J. M. 2010 Axisymmetric simulations of libration-driven fluid dynamics in a spherical shell geometry. *Phys. Fluids* **22**, 086602.

Cébron, D., Laguerre, R., Noir, J. & Schaeffer, N. 2019 Precessing spherical shells: flows, dissipation, dynamo and the lunar core. *Geophys. J. Intern.* **219**, S34–S57.

Cortet, P.-P., Lamriben, C. & Moisy, F. 2010 Viscous spreading of an inertial wave beam in a rotating fluid. *Phys. Fluids* **22**, 086603.

Deville, M. O., Fischer, P. F. & Mund, E. H. 2002 *High-Order Methods for Incompressible Fluid Flow*. Cambridge University Press.

Dintrans, B., Rieutord, M. & Valdettaro, L. 1999 Gravito-inertia waves in a rotating stratified sphere or spherical shell. *J. Fluid Mech.* **398**, 271–297.

Echeverri, P. & Peacock, T. 2010 Internal tide generation by arbitrary two-dimensional topography. *J. Fluid Mech.* **659**, 247–266.

Fischer, P. F. 1997 An overlapping Schwarz method for spectral element solution of the incompressible NavierStokes equations. *Journal of Computational Physics* **133**, 84–101.

Fritts, D. C. & Alexander, M. J. 2003 Gravity wave dynamics and effects in the middle atmosphere. *Reviews of Geophysics* **41** (1).

Greenspan, H. P. 1968 *The theory of rotating fluids*. Cambridge University Press.

Guenel, M., Baruteau, C., Mathis, S. & Rieutord, M. 2016 Tidal inertial waves in differentially rotating convective envelopes of low-mass stars. I. Free oscillation modes. *A & A* **589**, A22.

He, J., Favier, B. & Le Dizès, S. 2025 Internal shear layers generated by a vertically oscillating cylinder in unbounded and bounded rotating fluids. *J. Fluid Mech.* **1015**, A38.

He, J., Favier, B., Rieutord, M. & Le Dizès, S. 2022 Internal shear layers in librating spherical shells: the case of periodic characteristic paths. *J. Fluid Mech.* **939**, A3.

He, J., Favier, B., Rieutord, M. & Le Dizès, S. 2023 Internal shear layers in librating spherical shells: the case of attractors. *J. Fluid Mech.* **974**, A3.

Hurley, D. G. & Keady, G. 1997 The generation of internal waves by vibrating elliptic cylinders. Part 2. Approximate viscous solution. *J. Fluid Mech.* **351**, 119–138.

Kerswell, R. 1995 On the internal shear layers spawned by the critical regions in oscillatory Ekman boundary layers. *J. Fluid Mech.* **298**, 311–325.

King, B., Zhang, H. P. & Swinney, H. L. 2009 Tidal flows over three-dimensional topography in a stratified fluid. *Phys. Fluids* **21**, 116601.

Koch, S., Harlander, U., Egbers, C. & Hollerbach, R. 2013 Inertial waves in a spherical shell induced by librations of the inner sphere: experimental and numerical results. *Fluid Dyn. Res.* **45**, 035504.

Le Bars, M., Cébron, D. & Le Gal, P. 2015 Flows driven by libration, precession,

and tides. *Annu. Rev. Fluid Mech.* **47**, 163–193.

Le Dizès, S. 2024 Critical slope singularities in rotating and stratified fluids. *Phys. Rev. Fluids* **9**, 034803.

Le Dizès, S. & Le Bars, M. 2017 Internal shear layers from librating objects. *J. Fluid Mech.* **826**, 653–675.

Lighthill, M. J. 1978 *Waves in fluids*. Cambridge University Press.

Lin, Y. & Noir, J. 2021 Libration-driven inertial waves and mean zonal flows in spherical shells. *Geo. Astro. Fluid Dyn.* **115**, 258–279.

Llewellyn Smith, S. G. & Young, W. R. 2003 Tidal conversion at a very steep ridge. *J. Fluid Mech.* **495**, 175–191.

Machicoane, N., Cortet, P.-P., Voisin, B. & Moisy, F. 2015 Influence of the multipole order of the source on the decay of an inertial wave beam in a rotating fluid. *Phys. Fluids* **27**, 066602.

Marks, C. J. & Eckermann, S. D. 1995 A three-dimensional nonhydrostatic ray-tracing model for gravity waves: formulation and preliminary results for the middle atmosphere. *J. Atmos. Sci.* **52**, 1959–84.

Mathis, S. 2009 Transport by gravito-inertial waves in differentially rotating stellar radiation zones. I - Theoretical formulation. *A & A* **506**, 811–828.

Mirouh, G. M., Baruteau, C., Rieutord, M. & Ballot, J. 2016 Gravito-inertial waves in a differential rotating spherical shell. *J. Fluid Mech.* **800**, 213–247.

Moore, D. W. & Saffman, P. G. 1969 The structure of free vertical shear layers in a rotating fluid and the motion produced by a slowly rising body. *Phil. Trans. R. Soc.* A **264**, 597–634.

Munk, W. & Wunsch, C. 1998 Abyssal recipes ii: energetics of tidal and wind mixing. *Deep-Sea Res.* **45**, 1977–2010.

Ogilvie, G. I. 2005 Wave attractors and the asymptotic dissipation rate of tidal disturbances. *J. Fluid Mech.* **543**, 19–44.

Prat, V., Lignières, F. & Ballot, J. 2016 Asymptotic theory of gravity modes in rotating stars. I. Ray dynamics. *A & A* **587**, A110.

Prat, V., Mathis, S., Augustson, K., Lignières, F., Ballot, J., Alvan, L. & Brun, A. S. 2018 Asymptotic theory of gravity modes in rotating stars. II. Impact of general differential rotation. *A & A* **615**, A106.

St Laurent, L., Stringer, S., Garrett, C. & Perrault-Joncas, D. 2003 The generation of internal tides at abrupt topography. *Deep-Sea Res. I* **50**, 987–1003.

Thomas, N. H. & Stevenson, T. N. 1972 A similarity solution for viscous internal waves. *J. Fluid Mech.* **54**, 495–506.

Tilgner, A. 2000 Oscillatory shear layers in source driven flows in an unbounded rotating fluid. *Phys. Fluids* **12**, 1101–11.

Voisin, B. 2003 Limit states of internal wave beams. *J. Fluid Mech.* **496**, 243–293.

Walton, I. C. 1975 Viscous shear layers in an oscillating rotating fluid. *Proc. R. Soc. Lond.* A **344**, 101–110.

Wunsch, C. 1975 Internal tides in the ocean. *Rev. Geophys. Space Phys.* **13**, 167–182.

Zhang, H. P., King, B. & Swinney, H. L. 2007 Experimental study of internal gravity waves generated by supercritical topography. *Phys. Fluids* **19**, 096602.